PERGAMON

International Journal of Heat and Mass Transfer 45 (2002) 4809–4822

International Journal of HEAT and MASS TRANSFER

www.elsevier.com/locate/ijhmt

PIV flow measurements for heat transfer characterization in two-pass square channels with smooth and 90° ribbed walls

S.Y. Son [1], K.D. Kihm *, J.-C. Han

Department of Mechanical Engineering, Texas A&M University, College Station, TX 77843-3123, USA

Received 16 November 2001; received in revised form 7 May 2002

Abstract

Particle image velocimetry (PIV) experiments have been carried out to study the correlation between the high-Reynolds number turbulent flow and wall heat transfer characteristics in a two-pass square channel with a smooth wall and a 90° rib-roughened wall. Detailed averaged velocity distributions and turbulent kinetic energy for both the main and the secondary flows are given for a representative Reynolds number (*Re*) of 30,000. The PIV measurement results were compared with the heat transfer experimental data of Ekkad and Han [International Journal of Heat Mass Transfer 40 (11) (1997) 2525–2537]. The result shows that the flow impingement is the primary factor for the two-pass square channel heat transfer enhancement rather than the flow turbulence level itself. The characteristics of the secondary flow, for example, vortex's shape, strength, rotating-direction and positions, are closely correlated with the wall heat transfer enhancements for both smooth and ribbed wall two-pass square channels. The rib-induced flow turbulence increases the heat transfer mainly because of the enhanced local flow impingement near the rib.

1. Introduction

Advanced gas turbine airfoils are subjected to high heat loads that escalate cooling requirements to satisfy the airfoil life goals. Both external and internal cooling techniques are used; the internal cooling uses the coolant airflow through serpentine passages inside a turbine blade to convectively extract heat from the blade body. The coolant air in the passage develops a complex turbulent flow, in particular near the blade tip region, where the flow abruptly changes direction by 180°.

A two-pass U-channel of a blown-up scale has been widely used to simulate the serpentine coolant passage near the blade tip region matching the flow Reynolds number. Metzger et al. [1] studied forced convection in two-pass smooth rectangular channels by varying the divider location and the gap at the 180° turn. Han et al. [2] studied the local heat/mass transfer distribution in two-pass square channels with smooth and 90° ribbed walls. Han and Zhang [3] studied the effect of rib angle orientation on local heat/mass transfer distribution in a three-pass rib-roughened channel. It was observed that the rib angle, rib orientation, and the sharp 180° turn significantly affected the local heat/mass transfer distributions. The combined effects of these parameters increased or decreased the heat/mass transfer coefficients after the sharp 180° turns. The detailed heat transfer coefficient in the two-pass square channel was reported using liquid crystal technique by Ekkad and Han [4]. Park and Lau [5] also investigated the sharp-turning flows in a two-pass square channel with smooth walls using the naphthalene mass transfer technique for a relatively low-Reynolds number of 5500. Rau et al. [6] studied the effect of ribs on heat transfer enhancement and flow distribution in a straight channel. They showed that the secondary flows, which were generated by the ribs, effect on the local heat transfer enhancement at the lateral walls.

Investigation of the fluid dynamics inside the 180° turning critical regions of coolant passages is necessary to properly understand the convection heat transfer since the two (heat transfer and fluid dynamics) are

* Corresponding author. Fax: +1-979-862-2418.
E-mail address: ken-kihm@tamu.edu (K.D. Kihm).
[1] Present address: National Center of Microgravity Research, Cleveland, Ohio, USA.

0017-9310/02/$ - see front matter
PII: S0017-9310(02)00192-8

Nomenclature

D_h	hydraulic diameter
DVR	dynamic velocity range
DSR	dynamic spatial range
d_e	diameter of particle image
$f^{\#}$	F-number of camera lens
l	dimension of field-of-view
M_o	optical magnification
N	number of pixels
Nu	Nusselt number
Nu_0	Nusselt number for a smooth and straight circular channel
Re	Reynolds number
TKE	two-dimensional turbulent kinetic energy
U_b	bulk mean velocity
U, V, W	instantaneous velocity components
$\overline{U}, \overline{V}, \overline{W}$	ensemble averaged velocity components
u, v, w	fluctuating velocity components

Greek symbols

Δt	laser pulse delay
Δ	grid size of evaluation window
ΔZ_0	laser light sheet thickness
ε	standard error of mean value
λ	laser light wavelength
σ	standard deviation
σ_u	minimum resolvable velocity in x-direction
ζ	ratio of out-of-plane displacement to laser sheet thickness
max	maximum values

closely correlated as heat and momentum transfer phenomena.

Tse and Stauber [7] and Liou and Chen [8] studied the turbulent flow characteristics of a smooth channel with a 180° sharp corner turning using two-dimensional laser Doppler velocimetry (LDV) measurements. Study of flow visualization in a smooth channel with a 180° sharp corner was reported for a near laminar flow condition ($Re = 2500$) by Liou and Chen [9]. They also presented heat transfer coefficient distributions and fluid flow field data measured by using thermocouple probes and LDV, respectively. Liou et al. [10] reported the thickness effect of the flow divider on the flows in a two-pass smooth square channel with a 180° sharp turn at the free stream Reynolds number of 12,000. They showed that the turbulent kinetic energy and convective mean velocity are closely related with the "regionally averaged" heat transfer coefficient after the turning region. They also presented the effect of rotation on the local heat transfer distributions and the fluid flow around a 180° turn of a two-pass smooth square channel at a Reynolds number of 10,000 in their more recent work [11]. Jang et al. [12] reported on the computational results of flow and heat transfer in two-pass channel for Reynolds number of 30,000. Especially, they studied the effect of the angled rib (60° inclined from the flow axis) on the channel surface heat transfer.

Eggels et al. [13] reported on turbulent channel flow measurement using the particle image velocimetry (PIV) technique. The accuracy of PIV measurements for turbulent channel flows was compared with pointwise measurement techniques including much higher spatial resolution that is temporally correlated at a fixed time. The PIV technique also improved the spatial resolution near the channel wall region. Schabacker et al. [14] first reported stereoscopic PIV measurement of the flow passage of a smooth wall U-channel. Also, they showed the rib effects on the flow characteristics [15]. In their both studies the near-wall region data was not sufficiently presented and no attempt was made to provide a correlative interpretation of their flow measurement data with available heat transfer results.

The main effort of the present study has been an attempt to interpret our PIV results to understand the detailed and complex turbulent flow patterns inside a two-pass U-channel and to physically explain the convective cooling by the correlation between the main and secondary turbulent flows and the heat transfer data previously measured by Ekkad and Han [4], using a liquid crystal technique.

2. Experiment

2.1. Test section

The test section geometry (Fig. 1) was adopted from the previous heat transfer study of a U-channel [4]. Fig. 1a shows a smooth wall U-channel of a 50.8 mm square flow passage ($D_h = 50.8$ mm), and Fig. 1b shows a rib-roughened wall U-channel of the same dimension. The channel cross-sectional dimension uncertainty is estimated to be $\pm 0.197\%$ or ± 0.225 mm.

The flow was delivered by a suction pump attached to the channel outlet. The length from the air inlet to the end wall ($x = X_0 = 0$) is $22D_h$ (hydraulic diameter), accounting for the extended section of $10D_h$ long attached to the test section shown in Fig. 1. Since no smooth converging inlet was used, the incoming flow is somewhat disturbed from an ideal plug flow and thus, the

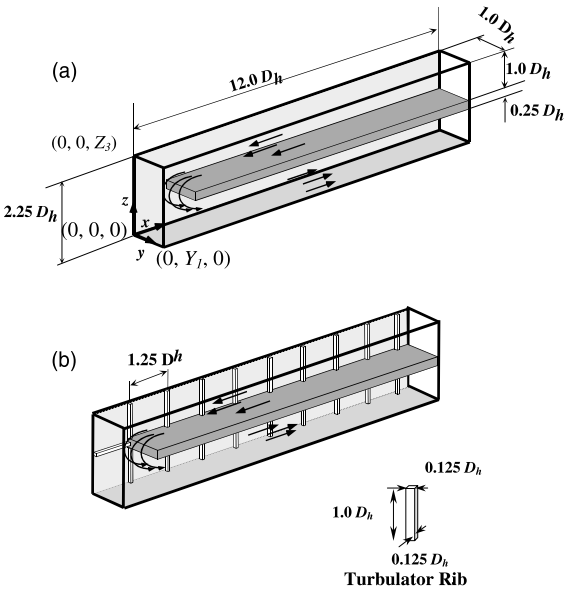

Fig. 1. Test sections: (a) smooth wall; and (b) 90° ribbed wall.

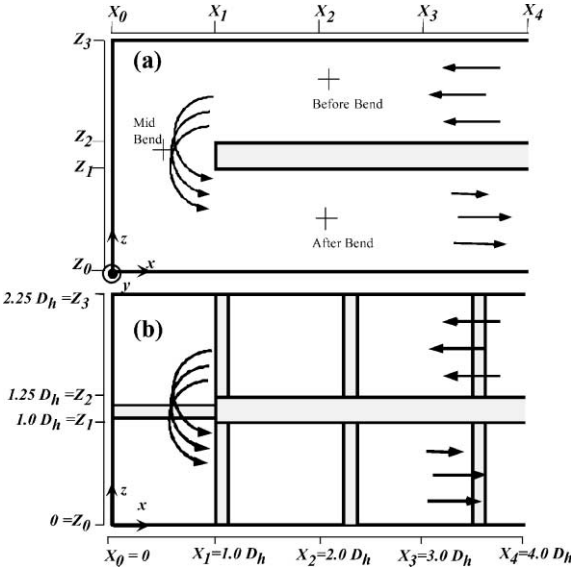

Fig. 2. Test section geometry for PIV measurement: (a) smooth wall; and (b) 90° ribbed wall.

fully developed length must be shorter than the well-known ideal value of the critical length of $L/D_h = 25$ for a converging inlet. Although not measured, we positively believe that the flow reached nearly the fully developed state at the measurement location.

The flow separator of $D_h/4$ thickness has 90° sharp edges providing 180° flow turning. The rib turbulators, a total of 19 attached to only one side wall, were made of a Plexiglas rod of $0.125D_h \times 0.125D_h$ cross-section with $1.25D_h$ intervals. Both channels were made of 12.7 mm thick Plexiglas. The inner wall surfaces, except for the optical access areas for the laser sheet and camera imaging, were painted with non-gloss black (approximately 250 μm in thickness) to reduce the laser light reflection from the glossy Plexiglas surfaces. The tested mean flow velocity $U_b = 3.49$, 8.73, and 16.00 m/s are corresponding to $Re = 12{,}000$, 30,000, and 55,000, respectively. This paper presents only the intermediate case of $Re = 30{,}000$ since the three cases are qualitatively similar [16]. The Reynolds number is calculated based on the air density and viscosity at 20 °C and on the length scale of D_h, and its uncertainty is estimated to be $\pm 2.45\%$ or $Re = 30{,}000 \pm 735$.

Fig. 2 shows the side-view of a tested U-channel with x- and z-coordinate marks for later reference in presenting the measurement results.

2.2. Particle image velocimetry system

The present PIV system consists of a Spectra Physics Model PIV-400 Nd:YAG double resonant tube laser providing frequency-doubled ($\lambda = 532$ nm) pulsed emissions of 400 mJ/pulse via a Q-switching module with a pulse duration of approximately 10 ns. The time delay between the two successive pulses was varied from 5 to 40 μs depending on the tested flow conditions. The seeding particles were generated by means of a Laskin type nozzle, which blows compressed air into the midst of corn oil forming air bubbles containing oil vapor that condenses to tiny oil droplets as the bubbles emerge to the oil–air interface and collapse. The mean diameter of the oil droplets was measured to be about 1 μm using the Malvern laser diffraction droplet analyzer [17], with specific gravity of 0.918, and refractive index of 1.464 [18]. A combination of two cylindrical lenses and a spherical lens collimated the laser light sheet of approximately 1 mm thickness at the measurement regions. The cooled full-frame interline-transfer $1280 \times 1024 \times 12$ bit CCD camera was used for recording particle images. The 1280×1024 imager CCD chip has an 8.70 mm × 6.96 mm dimension and the size of each pixel, $d_r = 6.8 \times 6.8$ μm. The field-of-view of PIV images was set as $(l_x = 114.3 \text{ mm}) \times (l_z = 114.3 \text{ mm})$ for the main flow measurement (on the xz-plane) and $(l_y = 50.8 \text{ mm}) \times (l_x = l_z = 50.8 \text{ mm})$ for the secondary flow measurement (on the yz- and the xy-plane). A Nikon 55 mm manual lens with $f^{\#} = 4.0$ was attached to the CCD camera with its magnification $M_o = 0.061$ and 0.137 for the main and the secondary flow measurements, respectively. A commercial LaVision FlowMaster-3 software system was used for the image recording, time synchronization control between the laser, and the CCD camera, and data processing.

The standard cross-correlation scheme based on FFT, developed by LaVision, Inc., was used to process the PIV

images to obtain the raw vector field. The scheme also implements a multi-pass interrogation process with an adaptive window offset algorithm to enhance the signal-to-noise ratio. The use of the window offset also improves the spatial resolution by effectively reducing the interrogation window size [19]. The first-pass cross-correlation is calculated for a 64×64-pixel interrogation window by FFT without window offset, and then the interrogation window is divided to four sub-areas of 32×32-pixel size for the second-pass calculation. The estimated displacement value (integer number) obtained from the first-pass calculation is used as the window offset value for the second-pass calculation. The displacement values of the four highest cross-correlation peak locations, corresponding to the four interrogation windows of the second-pass calculation, are stored for further vector validation processes. The 32×32-pixel square window corresponds to approximately 3.26 mm square grid for the main flow, and 1.59 mm square grid for the secondary flow in the physical plane.

The out-of-plane particle motion causes loss of particle image pairs and is the bias source in the determination of particle displacement in an interrogation window. When choosing the pulse delay (Δt) and the laser light sheet thickness (ΔZ_0), the out-of-plane motion should be considered in order to optimize the PIV turbulent experiment. Keane and Adrian [20] suggested one-quarter rule in deciding the optimal pulse delay where the ratio of the out-of-plane displacement to the laser sheet thickness must be smaller than 0.25, i.e., $\zeta = |W|\Delta t/\Delta Z_0 \leqslant 0.25$, where $|W|$ is the velocity magnitude, which travels in a cross-direction to the laser light sheet. The maximum range of the ratio ζ for the present experiment is calculated to be 0.175 for the main flow measurements on the x–z-plane (the laser sheet thickness $\Delta Z_0 = 1$ mm, instantaneous maximum of the secondary flow, $|W|_{\max} = 8.75$ m/s ($Re = 30,000$) in the out-of-plane direction of the main flow, and the typical pulse delay $\Delta t = 20$ μs), and 0.164 for the secondary flow measurements ($\Delta Z_0 = 1$ mm, instantaneous maximum of the main flow, $|U|_{\max} = 16.35$ m/s, which is corresponding to the out-of-plane direction for the secondary flow, and the typical pulse delay $\Delta t = 10$ μs). Note that the main flow measurement on the mid-plane ($y = 0.5D_h$) for the case of the smooth walled channel reduces the out-of-plane displacement error because of the flow symmetry on the mid-plane. For the secondary flow measurements, the error is inevitable and the pulse delay has been minimized because of the main flow crossing the secondary flow measurement plane.

2.3. Dynamic velocity range and dynamic spatial range

Dynamic velocity range (DVR) specifies the range of velocity variation over which measurements can be made. The instantaneous velocity magnitude, for the case of the smooth channel and $Re = 30,000$, ranges up to $U_{\max} = 16.35$ m/s for the main flow and 8.75 m/s for the secondary flow, occurring near the flow impingement region after the 180° turn. The maximum velocity ranges remained approximately the same for the roughened wall case. The DVR of the PIV system was estimated using the theory developed by Adrian [21], where DVR is defined as the ratio of the maximum velocity to the minimum resolvable velocity, or equivalently the rms error in the velocity measurement, i.e.,

$$\mathrm{DVR} = \frac{U_{\max}}{\sigma_u} = \frac{U_{\max}}{\sigma_{\Delta X} M_o^{-1} \Delta t^{-1}} \tag{1}$$

where the image magnification $M_o = 0.061$ for the main flow, and the laser pulse interval $\Delta t = 40$ μs (maximum interval used for the experiment). The rms error of the displacement on the pixel plane $\sigma_{\Delta X}$ is asserted as 4% of the recorded image diameter, i.e.,

$$\sigma_{\Delta X} = 0.04(d_e^2 + d_r^2)^{1/2} \tag{2}$$

where $d_r = 6.8$ μm represents the resolution of the recording medium that is taken to be equivalent to the pixel size, and d_e is the diameter of the particle image prior to being recorded on the pixel plane.

Assuming that the particle image is diffraction limited and its image intensity is Gaussian, the diameter of the diffracted image of the particle is expressed as [22]:

$$d_e^2 = M_o^2 d_p^2 + [2.44(1 + M_o) f^{\#} \lambda]^2 \tag{3}$$

where the seeding particle diameter $d_p = 1$ μm, the F-number of the imaging lens $f^{\#} = 4.0$, and the laser wavelength λ is taken as 532 nm. Thus, the recorded image diameter $(d_e^2 + d_r^2)^{1/2}$ is calculated to be 8.79 μm occupying approximately 1 pixel. Substituting Eq. (3) into Eq. (2) gives $\sigma_{\Delta X} = 0.35$ μm, and subsequently, the rms velocity measurement error $\sigma_u = 0.146$ m/s, and Eq. (1) gives DVR = 113. Similarly, DVR can be estimated to be 33 for the secondary flow measurement with $M_o = 0.137$ and $\Delta t = 10$ μs.

Dynamic spatial range (DSR) is defined as the ratio of the maximum resolvable scale to the minimum resolvable scale, i.e.,

$$\mathrm{DSR} = \frac{l}{\Delta x_{p\,\max}} = \frac{L_x/M_o}{U_{\max}\Delta t} \tag{4}$$

where the CCD pixel array dimension $L_x = 8.70$ mm, and DSR = 218 and 728 for the main flow and the secondary flow, respectively.

2.4. Data uncertainty of PIV measurement

In order to meet the statistical requirements for the mean and fluctuation velocity component measurements, a sufficient number (N) of PIV images must be recorded and processed. The probability distribution

Table 1
Uncertainties of ensemble averaged flow components at $Re = 30,000$

	Smooth wall	Ribbed wall
$\overline{U}$	$\pm 2.317 \times 10^{-2} U_b$	$\pm 2.974 \times 10^{-2} U_b$
$\overline{V}$	$\pm 2.586 \times 10^{-2} U_b$	$\pm 2.521 \times 10^{-2} U_b$
$\overline{W}$	$\pm 2.152 \times 10^{-2} U_b$	$\pm 3.927 \times 10^{-2} U_b$
TKE	$\pm 8.971 \times 10^{-3} U_b^2$	$\pm 4.368 \times 10^{-2} U_b^2$

function (PDF) of measured velocity magnitudes approaches a Gaussian when N is large, and the mean or ensemble averaged value approaches to a true mean as N goes to infinite. In the case of finite N-samplings of fluctuating property, such as instantaneous velocity vectors, their ensemble average bears an uncertainty from the true value. The central limit theorem [23,24] shows that the uncertainty can be approximately equal to the standard deviation of measured values (σ) divided by $\sqrt{N}$, i.e., the *standard error* of mean value, $\varepsilon = \sigma/\sqrt{N}$. Table 1 shows standard errors calculated from measured data for the velocity components $\overline{U}, \overline{V}$, and $\overline{W}$, and turbulent kinetic energy (TKE) averaged from 1000 PIV image data. The tabulated uncertainties are estimated at the locations of the highest standard deviations of the individual components, and they are equivalent to 95% confidence interval, which is equivalent to $\pm 1.96\sigma$. Note that the most uncertainties are smaller than 5%, for the case of TKE for the rib-roughened channel.

The selection of 1000 realizations is based on the examination of the data convergence with the number of PIV realizations. Fig. 3 shows ensemble averaged streamwise velocity ($\overline{U}/U_b$) and streamwise turbulence intensity ($\sqrt{\overline{u^2}}/U_b$) calculated for up to 2000 PIV realizations for the smooth wall U-channel flow at $Re = 30,000$. The three locations are selected as before-bend $(x_2, y_1/2, (z_2 + z_3)/2)$, mid-bend $x_1/2, y_1/2, (z_1 + z_2)/2)$, and after-bend $(x_2, y_1/2, z_1/2)$, representing the lower, medium, and higher turbulence level regions, respectively (Fig. 2). All the mean velocities and the lower turbulent flow data, the convergence lines are quite stable after 500 realizations. However, the data taken at the after-bend point of the highest turbulence, fluctuates until it reaches its asymptotic level of 34% near 1000 realizations. Therefore, all of the presented results are based on the ensemble average of 1000 PIV image pairs.

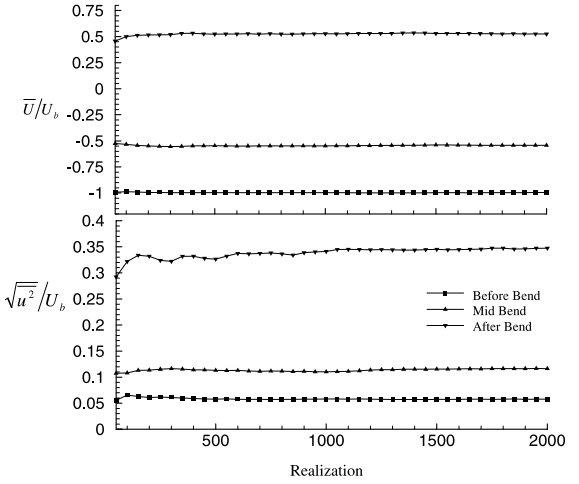

Fig. 3. Statistical convergence of ensemble averaged streamwise velocity $\overline{U}/U_b$ and turbulent intensity ($\sqrt{\overline{u^2}}/U_b$) depending on the number of PIV images taken for smooth wall at $Re = 30,000$.

3. Results and discussion

3.1. Correlation between heat and momentum transfer for smooth wall two-pass channels

3.1.1. Flow recirculation bubbles

Fig. 4 shows the average main flow velocities $(\overline{U}, \overline{W})$ and the average two-dimensional turbulence kinetic energy (TKE) levels ($100 \times ((\overline{u^2} + \overline{w^2})/2)/U_b^2$), which were evaluated from 1000 PIV images taken at the mid-plane ($y = 0.5Y_l = 0.5D_h$). The turning flow velocity magnitudes radially decrease with increasing radius to counterbalance the centrifugal force considering the inviscid

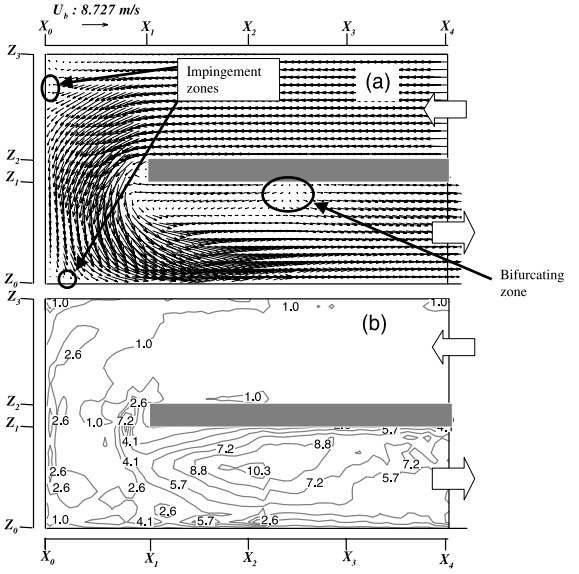

Fig. 4. Main flow development at $y = 0.5Y_l = 0.5D_h$ with smooth wall at $Re = 30,000$: (a) mean flow vector distribution averaged for 1000 PIV images; and (b) normalized turbulent kinetic energy $(((\overline{u^2} + \overline{w^2})/2)/U_b^2) \times 100$ distribution.

Euler momentum conservation. The sharp-tip separator drives an abrupt redirection of the flow with pressure reduction that induces a flow recirculation at the tip. The shear between the reversing flow and the main flow contributes to the local increase of TKE up to 7.2% near the tip of the flow separator (Fig. 4b). The 180° turning pushes the flow outward creating adverse pressure gradient in the inner region and creates a larger flow recirculation along the separator wall in the second-pass of the channel. The recirculation bubble extends from $x = X_1 - 0.2D_h$ to $x = X_2 + 0.4D_h$ and occupies $0.3D_h$ at maximum thickness. The reverse flow magnitude in the recirculation bubble reaches as high as one-half of the bulk mean speed, $0.5U_b$. Again, high values of TKE, up to 10.3% in Fig. 4b, are shown at the recirculation bubble boundary where the maximum reversing shear exists between the main flow and the recirculating flow. Note that the recirculation bubble zone on this mid-plane does not show any reattachment back to the separator wall, as shown in Fig. 4a. Instead, the flow is "bifurcating", apparently similar to a flow source point, from the separator wall near the maximum shear point. It is evident that to satisfy the mass continuity the flow must be induced into the mid-plane point by way of secondary flows from off-centered planes. This manifests complicated three-dimensional secondary flows, existing in the bubble area.

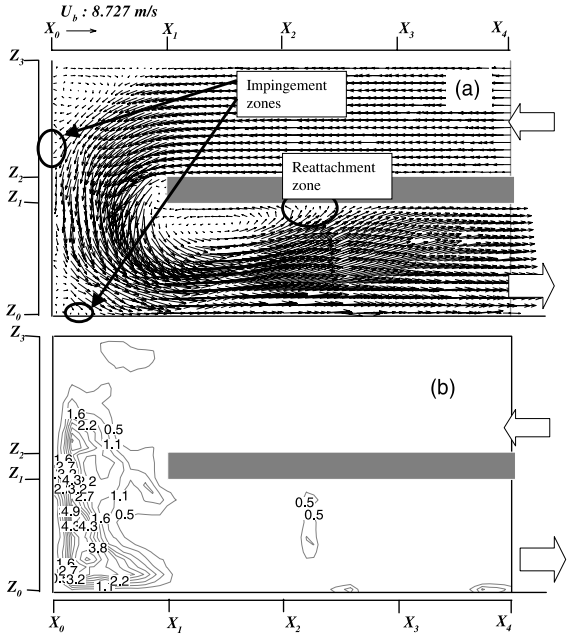

Fig. 5. Main flow development at $y = 0.125Y_1$ with smooth wall at $Re = 30,000$: (a) mean flow vector distribution averaged for 1000 PIV images; and (b) normalized turbulent kinetic energy $(((\overline{u^2} + \overline{w^2})/2)/U_b^2) \times 100$ distribution.

Fig. 5 shows the averaged main flow velocity and TKE distributions, which were measured at the off-center plane ($y = 0.125D_h$), close to the solid side wall ($y = 0$). Compared to the mid-plane ($y = 0.5D_h$) results shown in Fig. 4, the recirculation bubble region is more distinctive and stronger showing a clear reattachment of the flow onto the separator wall (Fig. 5a). Evidence from the flow field results in Figs. 4 and 5 and from additional results, measured at several different y-planes though not presented in the present paper, it is believed that the stronger flow recirculation developed near the side wall reattaches to the separator surface location off the mid-plane and the two reattached flows from both sides merge into the mid-plane to create the bifurcating flow, as previously discussed in Fig. 4a. The TKE measured at the plane closer to the side wall (Fig. 5b) shows a noticeable decrease compared with that at the mid-plane. Also, reversing shear that dramatically increases TKE in the mid-plane (Fig. 4b) is not shown in this off-mid-plane.

3.1.2. Flow impingement zones

Coming back to the mid-plane results shown in Fig. 4, the flow impingement onto the end wall ($x = X_0$) before turning provides a stagnation point at $z = Z_2 + 0.6D_h$ (Fig. 4a). The main flow splits from this stagnation point and induces a recirculation bubble near the upper left corner. Indeed, supplemented from our additional measurement results that are not presented, the impinging flow also splits into the lateral y-direction and contributes to the secondary flow formation. As the boundary layer thickness diminishes near the stagnation point, heat transfer enhancement is expected due to the high temperature gradient. The TKE level is somewhat quenched below 2.6% at the impingement zone. Another impingement is observed near the lower left corner at $x = X_0 + 0.18D_h$ and a local increase of heat transfer is expected to occur near this impingement location. The TKE level is again low at 1.0%, near the impingement zone.

For the plane closer to the sidewall (Fig. 5a), the impingement location is shifted to $0.8D_h$ below the upper left corner, before turning, and to $0.3D_h$, after turning. Because of the presence of the side wall, the overall TKE levels (Fig. 5b) are lowered compared with the previous mid-plane results. The quenching of TKE near the impingement locations is persistent and heat transfer enhancement near the impingement is also expected.

3.1.3. Correlation with heat transfer data

Fig. 6a shows a recreation of Nu/Nu_0 data previously published by Ekkad and Han [4] where they measured Nusselt number distributions on the side wall for the same test section geometry (except for the sepa-

rator leading edge shape), and with the identical flow conditions, using a liquid crystal technique. $Nu_0 = 0.023Re^{0.8}Pr^{0.4}$ [25] represents the fully developed turbulent flow Nusselt number for a smooth and straight circular tube. The high Nusselt number regions (solid arrows) approximately correspond to the impingement zones shown in Figs. 4 and 5. Another observed region of high heat transfer is located at the lower-channel wall (block arrow), after the impingement location, where the heat transfer increase is attributed to the large, main flow velocity gradients occurring due to the thin boundary layer development after the impingement while the main flow speed is accelerating.

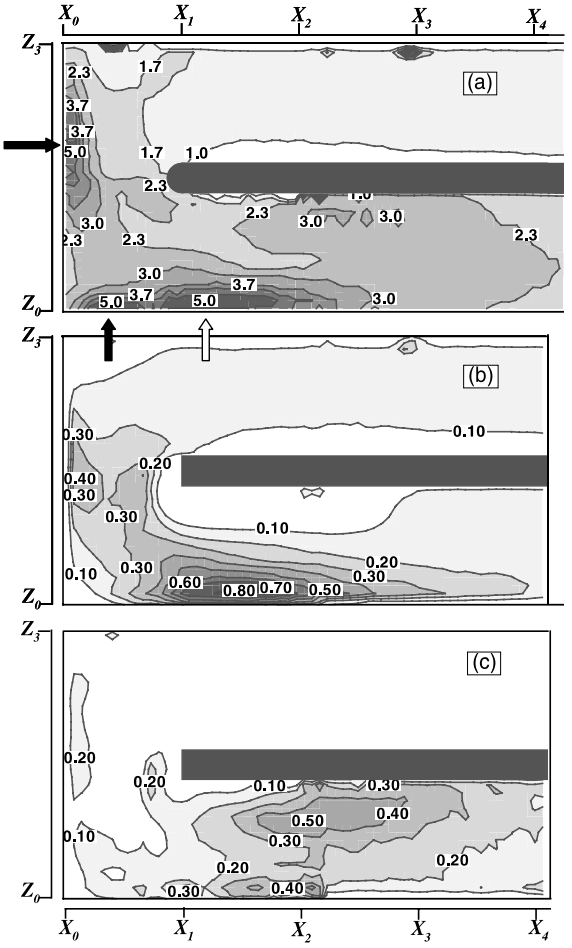

Fig. 6. Heat transfer coefficient (Nu/Nu_0) developments and heat-fluid correlations for the smooth wall U-channel at $Re = 30,000$ using the PIV data measured at $y = 0.5Y_1$: (a) heat transfer coefficient (Nu/Nu_0) distribution (recreated using the data presented in [4]); (b) correlation distribution between mean velocity and Nu/Nu_0; and (c) correlation distribution between TKE and Nu/Nu_0.

An attempt has been made to spatially correlate the mid-plane flow field data (Fig. 4) with the heat transfer data (Fig. 6a) to generate a mean flow heat transfer correlation $(\sqrt{U^2+W^2}/(\sqrt{U^2+W^2})_{\max})(Nu/Nu_0)$, and a TKE–heat transfer correlation, $(\mathrm{TKE}/\mathrm{TKE}_{\max})(Nu/Nu_0)$. The correlation values will be large if the magnitudes of the two properties, mean flow–Nusselt number or TKE–Nusselt number, are both large within the spatially coincidental range. Also, the high correlation of flow properties with heat transfer distribution will generate the contour map of the flow–heat correlation to be similar to the contour map of the heat transfer distribution, Nu/Nu_0. Thus, the mean flow–heat transfer correlation (Fig. 6b), in comparison with Fig. 6a, shows a fairly high level of correlation between the convection heat transfer and the mean flow distribution. This implies that the heat transfer enhancement can be largely attributed to the mean flow characteristics, including the local flow impingement and the high velocity gradients occurring from a thin boundary layer growth after the impingement. On the other hand, the TKE–heat transfer correlation (Fig. 6c) shows less consistent correlation between the heat transfer characteristics and the TKE level distribution at the mid-plane.

The similar correlation results (Fig. 7) calculated by using the PIV data measured closer to the channel side surface at $y = 0.125Y_1$ shows no distinctively different characteristics compared with the correlation using the mid-plane PIV data presented in Fig. 6. The mean flow–heat transfer correlation shows persistently higher level of correlation than the TKE–heat transfer correlation. The contour discontinuity shown in the middle of both the upper- and lower-passes in Fig. 7b is attributed to the artifacts that are resulted from "mismatching" of two PIV imaging field-of-views of approximately $2D_h \times 2D_h$ in dimension. (Note that a lower magnification or a single and bigger field-of-view was used to record images in Fig. 6 that does not show the trace of any mismatching.)

3.1.4. Secondary flow development

Fig. 8 shows the mean secondary flow development of the Dean-type [26] counter-rotating vortices (the left column) and the corresponding two-dimensional TKE (the right column), measured at different cross-sectional planes. The Dean-type vortex pair symmetrically develops along a curved smooth pipe or channel as the relatively faster inner flow carries a larger centrifugal force than the outer flow and this leads to the emergence of a secondary flow directing outwards in the center and inwards near the wall. The inset figures of the center column show the heat transfer data, Nu/Nu_0 measured along the side wall surface by Ekkad and Han [4].

The strong vortex pair appears at the 90°-turning plane from the incident flow direction (Fig. 8a) due to

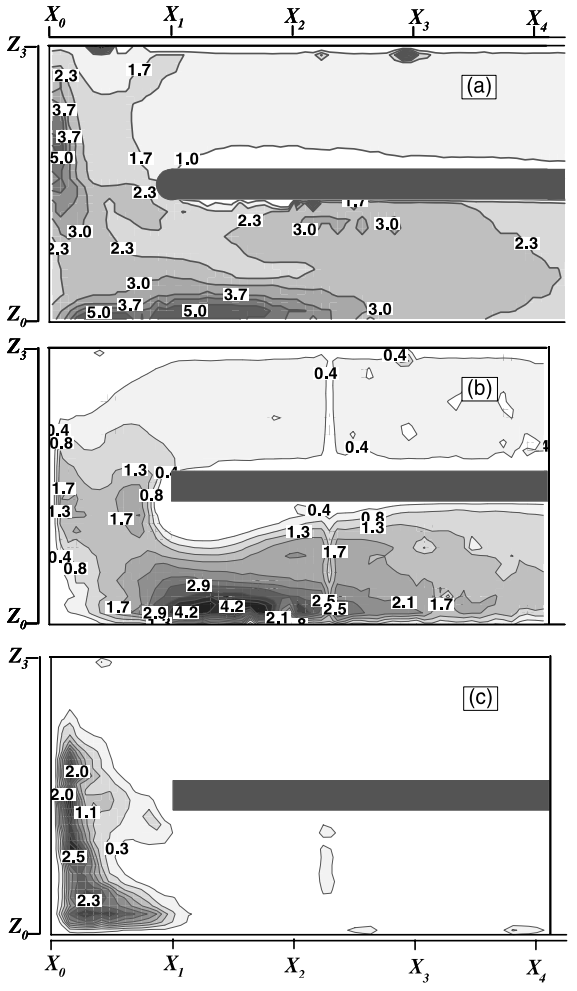

Fig. 7. Heat transfer coefficient (Nu/Nu_0) developments and heat-fluid correlations for the smooth wall U-channel at $Re = 30,000$ using the PIV data measured at $y = 0.125Y_1$: (a) heat transfer coefficient (Nu/Nu_0) distribution (recreated using the data presented in [4]); (b) correlation distribution between mean velocity and Nu/Nu_0; and (c) correlation distribution between TKE and Nu/Nu_0.

the centrifugal force action, then the vortex strength further increases with more flow turning at the 180°-turning plane (Fig. 8b), and then diminishes in the second-pass channel cross-sections (Fig. 8c and d). Note that the source-like bifurcating zone (circled region) shown at the upper middle region of Fig. 8b shows the reverse flow of the aforementioned recirculation bubble near the separator leading edge (Fig. 4a). In the plane $x = X_2$ (Fig. 8c), approximately $0.5D_h$ below the top (Z_1) along the symmetry line (the circled region on the center line), the secondary flow magnitude diminishes to conform a "virtual" source point. This region is adjacent to the bifurcating zone (Fig. 4a) where the bifurcating flow meets the main flow near the bubble boundary forming a stagnant-like region at $(x \sim X_2 + 0.4D_h, y \sim Z_1 - 0.3D_h)$. The downward flow from the top along the symmetry line in Fig. 8c and d is consistent with the development of the bifurcating flow shown in Fig. 4a. Fig. 8c and d also support the aforementioned finding in that the reattachment occurring off the mid-plane (block arrows) and the two reattached flows merge into the mid-plane to create the bifurcating flow.

3.1.5. Effect of impingement and recirculation on heat transfer

The locations of the maximum Nusselt number agree well with the impingement locations (solid arrows) on the side wall ($X_0 - X_1$ surface for Fig. 8a, and $Z_0 - Z_1$ surfaces for Fig. 8b and c). No distinctive maximum Nusselt number was observed for the case of no impingement shown in Fig. 8d. The maximum impingement velocity magnitudes, normalized by the bulk mean velocity U_b, are 0.24, 0.47, and 0.29 for Fig. 8a–c, respectively, and this can explain the main reason for the highest Nusselt number observed for the case of Fig. 8b.

While the flow impingement enhances the local convection heat transfer, a recirculation zone usually reduces heat convection since the flow is trapped inside the zone and the shear layer is formed between the separation zone and the main flow. Along the shear layer, thermal energy is transferred primarily by conduction [25]. The regions of noticeable reductions in the Nusselt number, following the impingement locations, are approximately identical to the recirculation bubble locations. Also, the small-scale sudden reduction of the Nusselt number very near the top and bottom corners, shown in almost all the cases, are attributed to the very tiny recirculation zones formed at the corners.

On the other hand, the large recirculation bubble along the flow separator (Fig. 4a) does not seem to directly contribute to reducing the heat transfer (Fig. 6a). The weaker vortex pair, shown above the Dean-type vortex pair, in Fig. 8c indicates that the flow inside the recirculation bubble reverses in two helical counter-rotating patterns. The resulting three-dimensional reverse flows accompanying the bifurcating flows near the flow source point (Fig. 8b and c) more aggressively transfer flow momentum across the bubble boundary without being trapped inside, unlike the normal two-dimensional recirculation zone. The relatively weaker vortices inside the recirculation zone counter-rotate with the stronger Dean-type vortices and the highest TKE levels are shown in the shear boundary of the two pair of vortices. This is consistent with the TKE contour plot shown in Figs. 4b and 5b. Further downstream, the weaker vortices are merged into the Dean-type vortices forming a single pair of two larger but relatively weaker vortex flows occupying the whole cross-section (Fig. 8d).

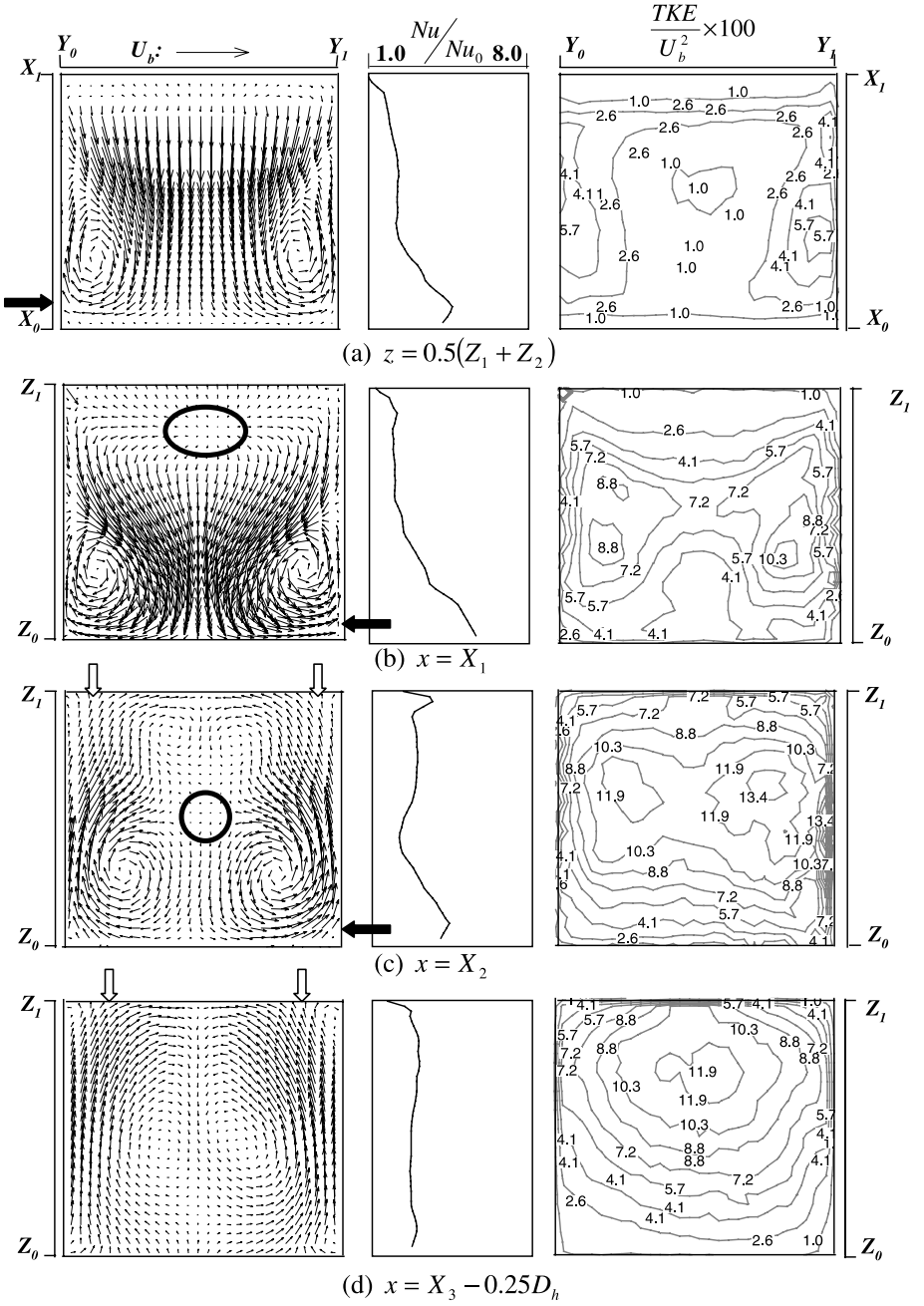

Fig. 8. Secondary flow development for smooth wall at $Re = 30,000$, ensemble-averaged from 1000 PIV images: (a) 90°-turning plane; (b) 180°-turning plane; (c) and (d) further downstream in the second-pass.

3.2. Correlation between heat and momentum transfer for ribbed wall two-pass channels

In comparison with the smooth wall case (Fig. 6a), the heat transfer enhancement for the ribbed surface is obvious as shown by the magnitude of the heat transfer coefficient Nu/Nu_0 in Fig. 9a (recreated from the data presented in [4]). The heat transfer enhancement is most distinctive around the rib area. In particular, the largest increase in the Nusselt number is observed on the top surface of each rib, followed by a sudden drop immediately after the rib and a fairly rapid recovery (solid arrows) of the Nusselt number before facing the next rib. This repeating pattern of Nusselt

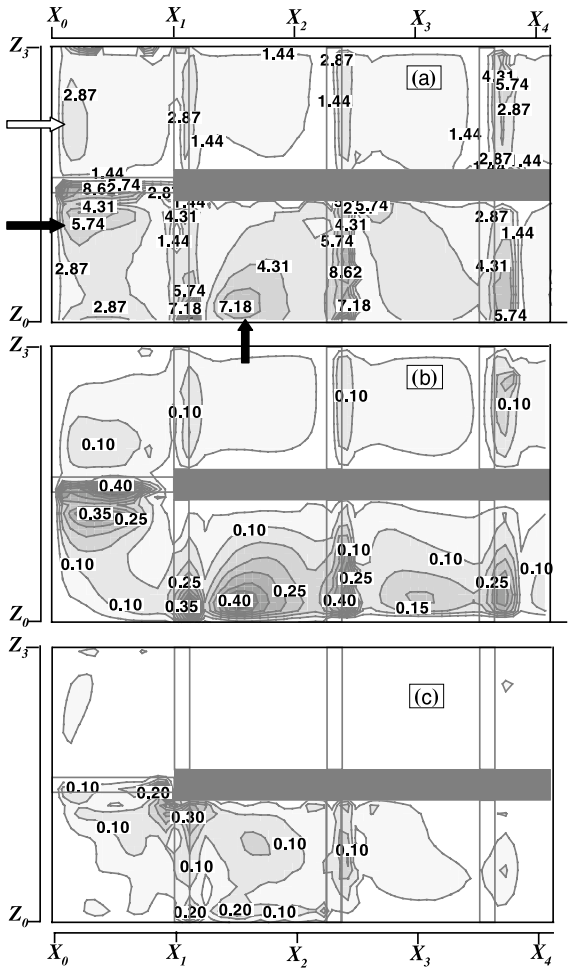

Fig. 9. Heat transfer coefficient (Nu/Nu_0) developments and heat–fluid correlations for 90° ribbed wall U-channel at $Re = 30,000$ using the PIV data taken at the mid-plane at $y = 0.5Y_1$: (a) heat transfer coefficient (Nu/Nu_0) distribution (recreated using the data presented in [4]); (b) velocity–magnitude vs. Nu/Nu_0 correlation; and (c) TKE vs. Nu/Nu_0 correlation.

number distribution is attributed to the main flow impingement on the rib and reattachment on the channel wall surfaces. The heat transfer increase at the upper end wall (block arrow) can also be explained by the flow impingement as previously discussed for the smooth wall case.

Fig. 9b shows the correlation between the Nusselt number distribution and the mean flow magnitude distribution in the mid-plane ($y = 0.5Y_1$). The high correlation near the top surface of each rib for the first (upper)-pass is attributed to the flow impingement and the resulting heat transfer enhancement. As the flow turns, generally higher correlations are achieved and the highest correlation point remains at the top surface of each rib. Note that heat transfer is higher near the outer wall than that near the inner wall (i.e., the flow separator wall) due to the strong flow impingement onto the outer wall while the turning. The direct impingement onto the upward-facing rib surface is reduced as the flow repeatedly passes the ribs. Additional high correlation points are located near the reattaching/impingement region on the sidewall immediately after the flow separation occurred by the protruding rib. This also shows high correlation compared with the Nusselt number results of Fig. 9a. The TKE results measured on the mid-plane show significantly less correlation with heat transfer distribution (Fig. 9c).

The heat and flow measurements for the region surrounding the three ribs in the second (lower)-pass are shown in Fig. 10. Fig. 10b shows the flow measurement for the mid-cross-section perpendicular to the rib where the 180° turned fast flow is rapidly deflected away from the first rib (block arrow) producing a flow separation and recirculation bubble behind the rib. The flow reattaches at $X_1 + 0.75D_h$ (solid arrow) and the main flow moves on to the second rib imposing a large shearing flow on the top surface of the second rib (circled region). This is believed to be the reason for the more distinctive increase in heat transfer at the top surface of the second rib, than the first rib, as shown in Fig. 9a. Note that the

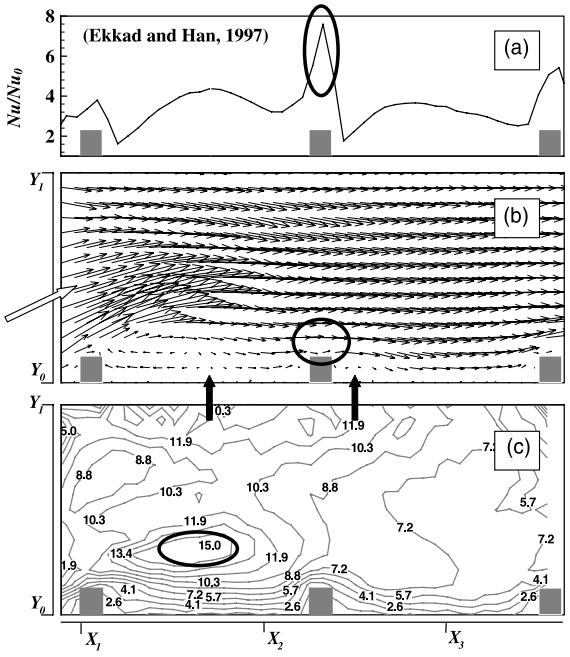

Fig. 10. Heat transfer distribution for the second-pass of the 90° ribbed channel and flow field development at $z = 0.5Z_1$ plane at $Re = 30,000$: (a) Nu/Nu_0 on the lateral wall; (b) flow vector plot at $z = 0.5Z_1$ plane; and (c) normalized turbulent kinetic energy, $(((\overline{u^2} + \overline{w^2})/2)/U_b^2) \times 100$ plot.

flow impingement to the upward-facing surface of the second rib is minimal. The flow passing the second rib is less disturbed, compared with the flow onto the first rib, since the disturbing effect from the flow turning is diminished, and thus, the flow separation is weaker and the recirculation zone reattaches closer to the rib, at $X_2 + 0.6D_h$ (solid arrow). The location of the local maximum heat transfer between the second and third ribs matches the reattaching impingement point. The turbulent kinetic energy contour (Fig. 10c) shows the

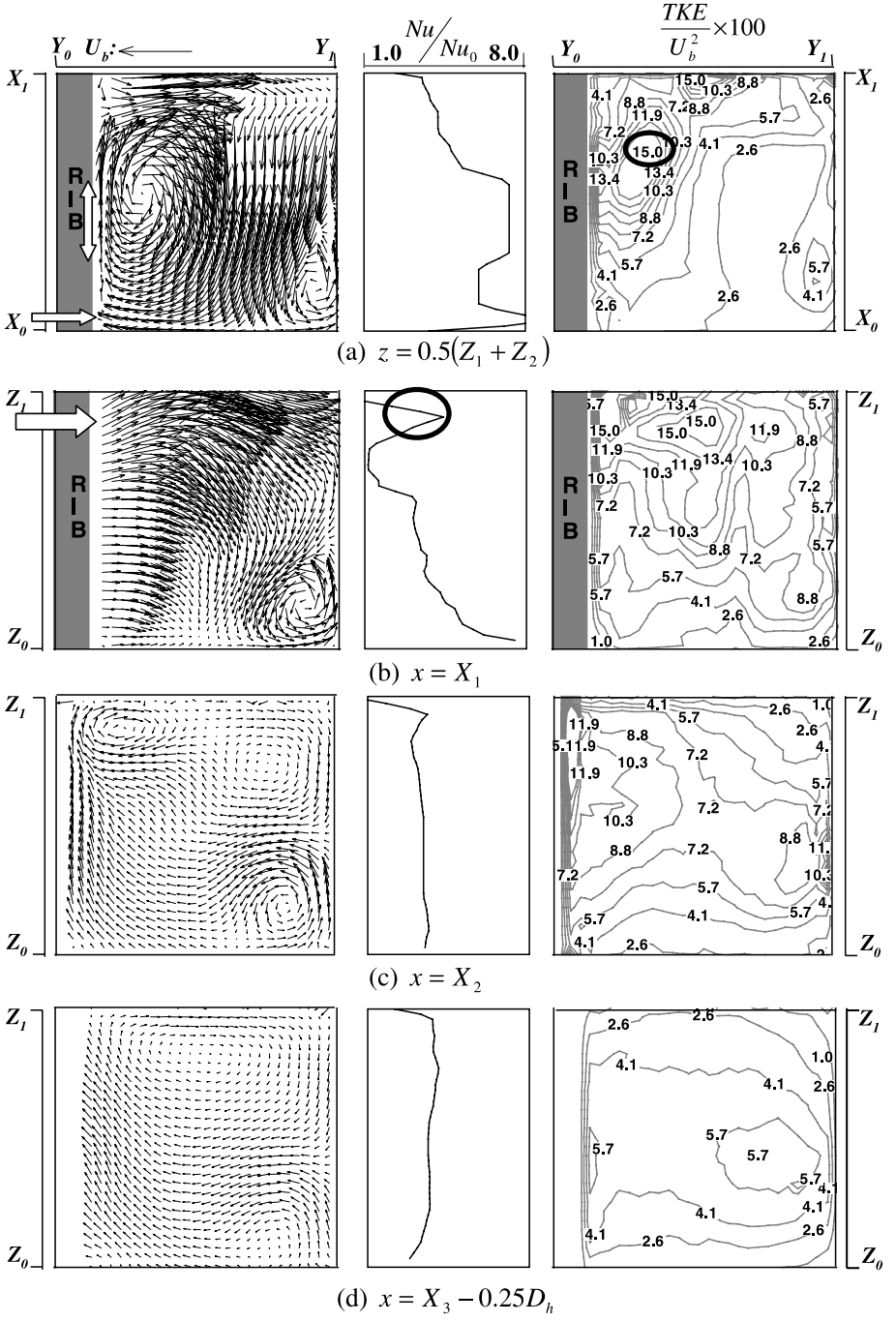

Fig. 11. Secondary flow development for 90° ribbed wall at $Re = 30,000$.

highest level (15%) occurring around the reversing shear layer created by the recirculating bubble and the main stream after the first rib (circled region). The TKE distribution, however, shows less persistent correlation with the heat transfer.

Fig. 11a shows the secondary flow on the cross-section at the 90° turn and the heat transfer distribution along the top surface of the rib. In comparison with Fig. 8a, the two Dean-type counter-rotating vortices are severely distorted in their sizes, strengths and locations, due to the asymmetry of the ribs attached to only one side wall, while they maintain their counter rotating directions. The highest heat transfer enhancement point matches the location of the impingement near the lower left corner (block arrow), whereas the highest TKE region is located above the mid-plane (circled region). The plateau region of high Nusselt number is attributed to the strong convection flow along the rib surface shown in the flow field distribution (double arrow). Fig. 11b shows the increasing Nusselt number, radially outward (Z_1 to Z_0), since the main flow velocity also radially increases and more convective heat transfer is expected on the top surface of the rib. In addition, the sharp peak in the heat transfer near the inner wall (circled region) is attributed to the rapid depletion of the secondary flow after the main flow impingement onto the upward surface of the rib (block arrow). No clear correlation of the TKE distribution is observed with respect to the heat transfer distribution. The Nusselt number further down stream, gradually recovers the spanwise uniformity as does the main flow. Flow vector fields shown in Fig. 11c and d are partially missing in the vicinity of the side wall (along Z_0 to Z_1) because of the physical blocking by the rib for optical access that is arranged through the end wall with an inclination angle.

Fig. 12 shows the tendency of heat transfer enhancement and TKE level in terms of the region-averaged Nusselt number and the region-averaged two-dimensional TKE for the main flow measured in the mid-plane. Regions were divided by the same section size (except for region 5) as illustrated in Fig. 12a. The summation of the regional Nusselt number of the 90° ribbed wall shows 33.8% higher heat transfer rate than the smooth wall, and the global TKE of the ribbed wall channel flow is 30.3% higher than the smooth wall. The smooth wall Nusselt number shows a sudden increase as the flow approaches the bend region (region 4), and continues increasing until region 6. After region 6, the Nusselt number remains unchanged until the completion of flow turning and then gradually decreases thereafter. However, the corresponding region-averaged TKE (Fig. 12c) has a gradual slope of growth from region 3 to region 6, and then a higher slope until region 8. It is shown that the region-averaged TKE less accurately correlates with the region-averaged heat transfer characteristics.

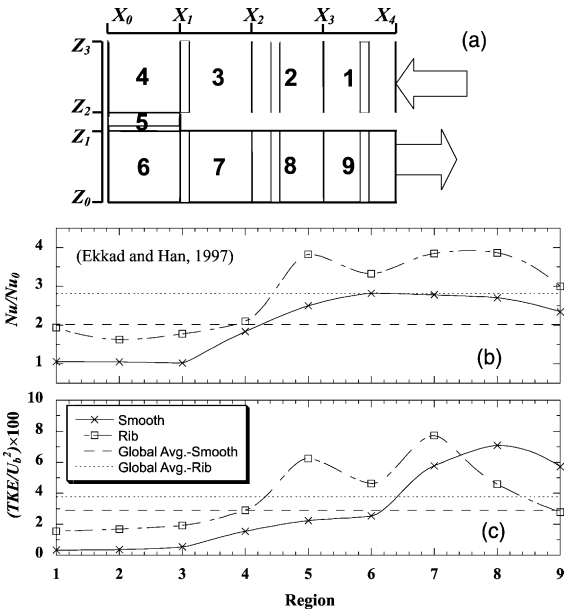

Fig. 12. Effect of the 90° ribs on the Nu/Nu_0 and normalized turbulent kinetic energy at $Re = 30,000$ using the PIV data measured at the mid-plane: (a) regions in the test section; (b) regionally averaged Nu/Nu_0; and (c) regionally averaged turbulent kinetic energy.

The Nusselt number for the ribbed surface is persistently higher than the smooth wall for all regions (Fig. 12b). The Nusselt numbers for regions 4 and 6 approach those of the smooth wall since the two regions do not have the ribbed top surface where the maximum Nusselt number is expected. The region-averaged TKE shows a higher level for the ribbed channel than for the smooth channel, except for regions 8 and 9, where the magnitudes are reversed. This may imply that the turbulence enhancing effect by the flow turning on the downstream flow is diminished more quickly for the ribbed wall channel and a faster recovery of the flow back to the straight ribbed-channel flow of the upstream condition may be expected. In contrast to the TKE variation, the Nusselt numbers in regions 8 and 9 are persistently higher than the smooth wall and this may be attributed to the stronger impingement induced by the stronger secondary flows as previously discussed in Fig. 11. This again supports our finding in that the flow impingement, rather than the flow TKE, is more contributing to the heat transfer enhancement of both smooth and ribbed U-channel flows.

4. Conclusion

PIV experiments have been carried out in order to study the detailed and localized effects of high-Reynolds

number flow ($Re = 30,000$) on heat transfer enhancement in a two-pass square channel with a smooth wall and a 90° rib-roughened wall. Primary conclusions that are achieved from the study are:

1. The flow impingement is the main factor for heat transfer enhancement in the two-pass square channel. The regions of flow impingement induced by the main flows (Figs. 4–7 and 9) or secondary flows (Figs. 8 and 11) are well matched with the regions of local heat transfer enhancement, respectively as shown in the same sets of the figures. On the other hand, the regions of higher flow turbulence level show weaker correlation with heat transfer enhancement.
2. Secondary flow characteristics, such as the vortex's shape, strength, rotating-direction and positions, are closely correlated with the wall heat transfer enhancement for smooth and ribbed wall two-pass square channels. The locations of high Nusselt numbers are consistent with the locations of strong vortex flow impingement onto the side surface.
3. For the smooth wall cases, there exist two pairs of counter-rotating vortices in the secondary flows. A pair of relatively weaker vortices is developed inside the flow separation zone along the separator, and another pair of stronger vortices is developed outside the flow separation zone (Fig. 8c). These two pairs of vortices tend to merge after the flow is reattached to the separator (Fig. 8d). In addition, the tiny vortices developed at each corner of the cross-sectional plane tend to locally decrease the heat transfer.
4. The 90° ribs cause the development of complicated three-dimensional secondary flows and enhanced flow turbulence levels. Nevertheless, the heat transfer enhancement for the ribbed wall is more directly identified by the locations of flow impingement on the upward-facing surfaces of the ribs, the enhanced shear of the main flow on the top surfaces, and the reattachment after the flow separation, next to the backward-facing surfaces.

References

[1] D.E. Metzger, M.K. Sahm, Heat transfer around 180° turns in smooth rectangular channels, ASME J. Heat Transfer 108 (1986) 500–506.

[2] J.C. Han, P.R. Chandra, S.C. Lau, Local heat/mass transfer distributions around sharp 180 deg. turns in two-pass smooth and rib-roughened channels, ASME J. Heat Transfer 110 (1988) 91–98.

[3] J.C. Han, P. Zhang, Effect of rib-angled orientation on local mass transfer distribution in a three-pass rib-roughened channel, ASME J. Turbomach. 113 (1991) 123–130.

[4] S. Ekkad, J.C. Han, Detailed heat transfer distributions in two-pass square channels with rib turbulators, Int. J. Heat Mass Transfer 40 (11) (1997) 2525–2537.

[5] C.W. Park, S.C. Lau, Effect of channel orientation of local heat (mass) transfer distributions in a rotating two-pass square channel with smooth walls, J. Heat Transfer 120 (1998) 624–632.

[6] G. Rau, M. Cakan, M. Moeller, T. Arts, The effect of periodic ribs on the local aerodynamic and heat transfer performance of a straight cooling channel, ASME J. Turbomach. 120 (1998) 368–375.

[7] D.G.N. Tse, G. Steuber, Flow in rotating serpentine coolant passages with skewed trip strips, NASA Contractor Report 198530 (1985) NAS3-27378.

[8] T.M. Liou, C.C. Chen, LDV study of developing flows through a smooth duct with a 180 deg. straight-corner turn, ASME Paper no. 97-GT-283, 1997.

[9] T.M. Liou, C.C. Chen, Heat transfer in a rotating two-pass smooth passage with a 180° rectangular turn, Int. J. Heat Mass Transfer 42 (1999) 231–247.

[10] T.M. Liou, Y.Y. Tzeng, C.C. Chen, Fluid flow in a 180 deg. sharp turning duct with different divider thickness, ASME J. Turbomach. 121 (1999) 569–576.

[11] T.M. Liou, C.C. Chen, M.Y. Chen, TLCT and LDV measurement of heat transfer and fluid flow in a rotating sharp turning duct, Int. J. Heat Mass Transfer 44 (2001) 1777–1787.

[12] Y.J. Jang, H.C. Chen, J.C. Han, Computation of flow and heat transfer in two-pass channels with 60 deg. ribs, J. Heat Transfer 123 (2001) 563–575.

[13] J.G.M. Eggels, F. Unger, M.H. Weiss, J. Westerweel, R.J. Adrian, R. Friedrich, F.T.M. Nieuwstadt, Fully developed turbulent pipe flow: a comparison between direct numerical simulation and experiment, J. Fluid Mech. 268 (1994) 175–209.

[14] J. Schabacker, A. Boelcs, V. Johnson, PIV Investigation of the flow characteristics in an internal coolant passage with two ducts connected by a sharp 180 deg. bend, ASME Paper no. 98-GT-544, 1998.

[15] J. Schabacker, A. Boelcs, V. Johnson, PIV Investigation of the flow characteristics in an internal coolant passage with 45 deg. rib arrangement, ASME Paper no. 99-GT-120, 1999.

[16] S.Y. Son, Stationary and unstationary turbulent flow measurements using particle image velocimetry (PIV), Ph.D. Thesis, Texas A&M University, College Station, TX, 2000.

[17] H.G. Barth, Modern Methods of Particle Size Analysis, Wiley, New York, 1984 (Chapter 5).

[18] M.W. First, S.N. Rudnick, X. Yan, Use of alternative liquids in laskin nozzle generated aerosols for filter testing, Am. Ind. Hyg. Assoc. J. 53 (1992) 242–247.

[19] J. Westerweel, D. Dabiri, M. Gharib, The effect of a discrete window offset on the accuracy of cross-correlation analysis of digital PIV recordings, Exp. Fluids 23 (1997) 20–28.

[20] R.D. Keane, R.J. Adrian, Optimization of particle image velocimeters, Part II: multiple pulsed systems, Meas. Sci. Technol. 2 (1991) 963–974.

[21] R.J. Adrian, Dynamic ranges of velocity and spatial resolution of particle image velocimetry, Meas. Sci. Technol. 8 (1997) 1393–1398.

[22] J.W. Goodman, Introduction to Fourier Optics, McGraw-Hill, San Francisco, 1996.

[23] R.L. Ott, An Introduction To Statistical Methods and Data Analysis, Duxbury Press, Belmont, California, 1993.
[24] W.M. Rohsenow, H. Choi, Heat, Mass and Momentum Transfer, Prentice-Hall Inc., New Jersey, 1961, pp. 192–193.
[25] E.R.G. Eckert, R.M. Drake, Analysis of Heat and Mass Transfer, McGraw-Hill, New York, 1972.
[26] H. Schlichting, Boundary-Layer Theory, seventh ed., McGraw-Hill, New York, 1979.